ELSEVIER

Contents lists available at ScienceDirect

International Journal of Multiphase Flow

journal homepage: www.elsevier.com/locate/ijmulflow



A method for measuring droplet evaporation in a shock-driven multiphase instability



Vasco Duke-Walker^a, Roy Allen^a, W. Curtis Maxon^a, Jacob A. McFarland^{a,b,*}

- ^a Mechanical and Aerospace Engineering, University of Missouri, Columbia, Mo USA
- ^b Mechanical Engineering, Texas A&M University, College Station, Tx USA

ARTICLE INFO

Article history:
Received 29 June 2020
Revised 31 August 2020
Accepted 13 September 2020
Available online 15 September 2020

Keywords: Evaporation Multiphase SDMI Q-PLIF

ABSTRACT

Experimental measurements of bulk droplet evaporation within a shock-driven multiphase instability, or SDMI, were studied using advanced imaging diagnostics. Specifically, droplet evaporation was quantified by determining the rate of acetone vapor produced from liquid acetone droplets. The extent of the acetone vapor produced was measured using quantitative planar laser-induced fluorescence (Q-PLIF). In addition to vapor concentration, Q-PLIF also accounts for the effects of pressure and temperature on the fluoresced acetone. Concurrently performed with Q-PLIF were particle image velocimetry (PIV) measurements as the means to gather data on the acetone droplet's velocities as well as the particle fields morphology throughout its development. By using these two diagnostic techniques, two successive data points of the acetone droplets evaporation rate throughout the development of the SDMI were obtained. Although these first two data sets were not adequate to fully prescribe an accurate evaporation rate model, they were a sufficient corrigendum to the commonly-utilized D-squared evaporation law. Overall, the previous techniques have been demonstrated that acetone droplet evaporation can be measured quantitatively, enabling prediction of evaporation enhancement due to the strong hydrodynamic mixing within the SDMI.

© 2020 Elsevier Ltd. All rights reserved.

1. Introduction

The SDMI develops when a high-speed shock wave instantaneously accelerates a multiphase flow field possessing steep gradients in reference to their multiphase parameters (e.g., mixture density, particle equilibration time). The multiphase field is composed of both a carrier phase, here a gas, and a dispersed particle phase, here liquid droplets. During the SDMIs evolution, the lighter carrier gas is accelerated instantaneously by the shock wave. At the same time, the heavier particle-phase remains initially unaffected wherein it lags behind the gas phase in both velocity and temperature, as well as in phase equilibrium. Thus, regions laden with higher concentrations of particles will have a momentum deficit that results in the generation of vorticity and thus large-scale mixing at steep gradients in particle properties. In the case of small, fast-reacting particles, the SDMI resembles the Richtmyer-Meshkov instability or RMI (Vorobieff et al., 2011; McFarland et al., 2016).

As the size of the particles increases, the equilibration time becomes comparable to the instability time-scales. The particle velocity equilibration time for a shock-driven flow can be defined as $t_v = d_p^2 \rho_p/(18\mu_g)$, where d_p is the droplet diameter, ρ_p is the den-

E-mail address: mcfarlandja@tamu.edu (J.A. McFarland).

sity of the particle, and μ_g is the viscosity of the gas Marble (1970). The relative length of the velocity equilibration time is often measured by the particle Stokes number, St, defined as the ratio of t_v to a characteristic time for the particle-gas flow. For the SDMI, the St, as traditionally defined, is not found to be the correct scaling (McFarland et al., 2016). Instead the velocity equilibration time may be compared to a characteristic time for the hydrodynamic instability.

The particles lag further behind the gaseous flow-field for larger velocity equilibration times, resulting in diminished vorticity development due to competition between the gas and particle timescales. These effects are unique to the SDMI (Middlebrooks et al., 2018). Therefore, the RMI may be considered as a limiting case for the SDMI, where the particle equilibration times are infinitesimally short. Further explanation of the RMI and how it differentiates from the SDMI is discussed next.

The RMI arises due to the interaction of an impulsive acceleration, often in the form of a shock wave, and a misaligned density gradient created by a fluid interface, which ultimately leads to the generation of vorticity. The linearity, or the ratio of perturbation amplitude to the mixing wavelength $(\frac{\eta}{\lambda})$, of the interface defines the extent of the misalignment. The lower this ratio is, the weaker the instability will be. For the limiting case of infinitesimally small particles, the primary driving parameter of the SDMI becomes the gradient of the effective density. Similar to the RMI,

Corresponding author.

the effective density gradient for a SDMI can be quantified by the effective Atwood number, $A_e = (\rho_{e_2} - \rho_{e_1})/(\rho_{e_2} + \rho_{e_1})$, where subscripts 1 and 2 denote the upstream and downstream multiphase fluid mixture's densities respectively and ρ_e is the effective density of the mixture which is defined as the total mass of carrier and particle-phase divided by the total volume these phases occupy.

The presence of the SDMI has been studied within various multiphase applications where phase change is a relevant phenomenon. In the case of, the particle phase consists of droplets, and we refer to it as such where the effects are unique to liquid particles (droplets). Shock-driven evaporating droplets have been studied in turbines to understand the phase change component between steam and water droplets and the effect on the overall performance of the turbomachinery (Wróblewski et al., 2009). In supersonic combustion, the SDMI drives the mixing and evaporation of liquid fuels with air, which occurs on the order of microseconds (McFarland and Hagenmaier, 2018). On a much larger scale, cosmic dust is processed and sublimated by shock waves such as those produced by asymptotic giant branch stars and supernovae. A description of the formation, time evolution, and evaporation of the dust particles provides a better understanding of interstellar dust and the star's life-cycle (Kozasa et al., 2009). Furthermore, multiphase shock interactions occur in many other applications such as ejector pumps (Colarossi et al., 2012), rotating detonation engines, and pulse detonation engines (Lu and Braun, 2014). These are but a few of the applications that exist where the SDMI is present.

1.1. Evaporation effects and measurement

Evaporation effects in the SDMI have been studied in previous simulation work (Dahal and McFarland, 2017; Black et al., 2017). These studies have found that evaporation increases large scale mixing by decreasing the particle sizes, and therefore, the equilibration times. Evaporation also increases A_e by cooling the carrier gas, due to the latent heat of vaporization, effectively increasing the carrier gas density. The increased density will act to enhance circulation and vorticity deposition for subsequent shock accelerations of the flow field. Consequently, the two main parameters driving evaporation were the diffusion coefficient, D_v , and saturation pressure, P_{sat} . D_v had little effect on the instability (i.e., morphology); however, it had a large effect on the evaporation rate. P_{sat} sets an upper limit for the amount of particle mass that can evaporate, and therefore, the late time A_e of the interface.

Evaporation rates were found for a spherical interface under similar conditions as Dahal and McFarland (2017); Black et al. (2017) in the computational study performed by Paudel et al. (2018). This work showed that the droplets' spatial distribution has a significant effect on the gas hydrodynamics and causes large variations in evaporation rates. Evaporation strongly depends on the initial radial location of the droplet in the interface and the gas hydrodynamics. As droplets become smaller, they react faster. Droplets on the outer surface of the spherical interface are entrained and mixed by the primary vortex ring and evaporate faster relative to droplets of a similar size in the core of the interface.

In experiments, droplet evaporation rates have been measured using several techniques. Water droplet evaporation rates were studied experimentally by Goossens et al. (1988). They proposed the differential quadrature (DQ) method or two-wavelength light extinction method to estimate the rate of evaporation. The DQ method allows for the determination of the mean droplet radius, mass density, and particle size distribution. This method strongly depends on the light extinction coefficient of two different wavelengths to predict the evaporation rate (i.e., droplet size changes due to shock propagation through the mixture). In this study, the droplets size was shown to decrease following the D-squared law,

or D^2 law. Unfortunately, this theory becomes invalid when particles' radii are $r_m > 1~\mu m$, due to its relative error in extinction coefficients and when the Weber number is more than five as droplets deformed and/or break into finer droplets.

In another study, Hanson et al. (2007) combined experimental data and computational results to develop a new empirical model in both continuum and non-continuum regimes for measuring the evaporation rate. The experimental results were obtained through extinction diagnostics and then compared with simulation. To increase the experimental accuracy and sensitivity, five different laser wavelengths were utilized. From the results, droplet evaporation rates seemed to deviate from the D^2 law, with the difference becoming more significant with droplet size smaller than 20 μ m. This model, however, has not been developed or validated further.

The methods listed so far rely on measuring the droplet sizes at any instance in time. This can be challenging in the presence of a distribution of droplets and is further complicated by heterogeneous spatial distributions (i.e., the interface morphology) created by the SDMI. For our research, we rely on the quantitative planar laser-induced fluorescence (Q-PLIF) measurement of vapor production, rather than the decrease in droplet size, to quantify evaporation rates. One evident drawback is that only bulk measurements of the evaporation rate may be acquired for all droplets of varying sizes. However, utilizing the Q-PLIF method has the advantages of: (1) being able to resolve the spatial distributions of vapor production, (2) being able to measure evaporation from a droplet field with a wide distribution of sizes, and (3) utilizing existing, proven imaging techniques. To perform Q-PLIF measurements, choosing an optimal tracer particle is required.

1.2. Diagnostics

Acetone is an ideal tracer for Q-PLIF imaging of gaseous flows due to high vapor pressure and low toxicity. Using a tracer with a high vapor pressure enables a higher vapor concentration in the gas phase, increasing the strength of the fluorescence signal. At room temperature, acetone vapor concentration is high enough to produce effective fluorescence measurements in atmospheric air (Thurber, 1999). Acetone fluoresces in the range of 350–550 nm and has an accessible absorption wavelength of 225–320 nm, with a peak near the Nd:YAG laser harmonic of 266 nm. This makes it ideal for the quantification of temperature, pressure, and concentration in gases. Thurber (Thurber, 1999) has performed a detailed study of acetones fluorescence dependence on temperature and pressure, which enables the correction of signal intensity variations due to these factors.

Q-PLIF and PIV methods have been used in a multitude of fluid experiments on the Richtmyer-Meshkov instability (RMI) (Christopher (2012); Orlicz. (2012); Mohammad (2019)). PIV is a non-intrusive technique that allows quantitative and qualitative measurements of the flow development in which two back-to-back images of the flow field are captured, separated by some short Δt = 2 μm difference in time Thielicke and Stamhuis (2014). Image analysis software is then used to find the correlation between the particle fields' patterns in each image, predicting the motion (velocity) of the particles between the two images.

In RMI experiments, vorticity deposition, the driving mechanism of RMI mixing (Orlicz., 2012), and gas mixing have been measured using the time evolution of the velocity (from PIV) and species (from Q-PLIF) fields. These experimental measurements have been performed over various shock strengths and initial conditions. The RMIs turbulent mixing characteristics were studied by Mohammad (2019). Utilizing simultaneous Q-PLIF and PIV measurements, these experiments allowed for the measurement of gas mixing and turbulent energy through multiple shock accelerations

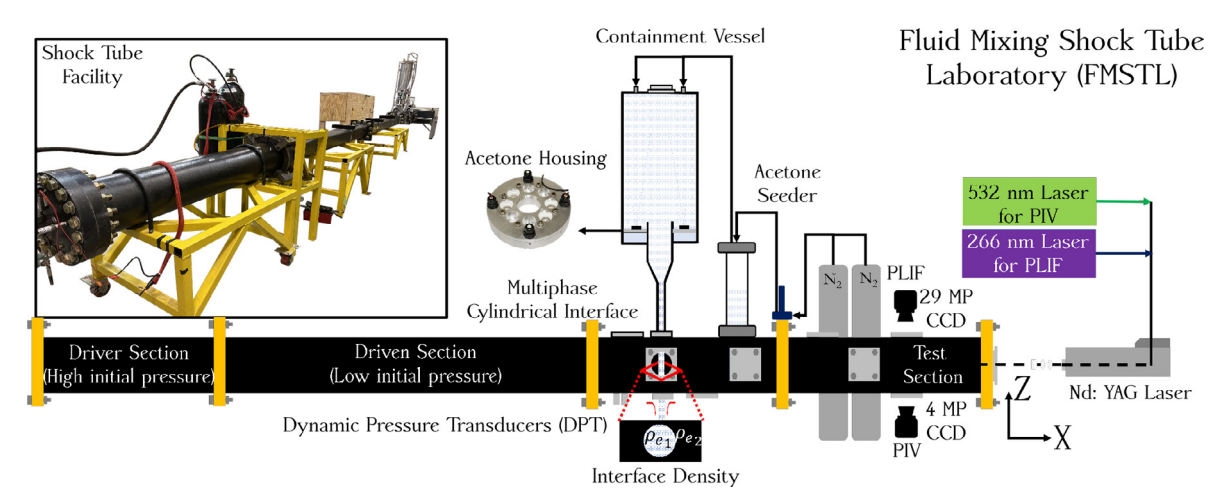


Fig. 1. Shock tube facility.

to determine the extent to which the Mach number affects turbulent mixing (Mohammad, 2019).

1.3. Break-up

Large droplets can deform and take on different shapes, or breakup into smaller (i.e., finer) droplets (child droplets) (Pilch and Erdman, 1987). This process enhances the droplet surface area and increases mass transfer between the particle and gas phases. The Weber ($We = (\rho_g (u_g - u_p)^2 d_p)/\sigma$), the Ohnesorge $(Oh = \mu_p / \sqrt{\rho_d d_p \sigma})$, and the Reynolds number $(Re_p =$ $ho_g(u_g-u_p)d_p/\mu_g)$ are all used to characterize the conditions surrounding the deformation and break-up of a droplet within a multiphase flow. These non-dimensional numbers rely on the following variables: the velocity of the particle (u_p) , the velocity of the gas (u_g) , the density of the gas (ρ_g) , the density of the droplet (ρ_d) , and the droplet's dynamic viscosity (μ_p). The We relates the hydrodynamic forces to the stabilizing forces of the droplet surface. Typically, droplet break-up is not predicted to occur below We ~ 12 (Middlebrooks, 2019). The Oh relates the viscous forces to the surface tension forces. In other words, at higher Oh droplets are less likely to breakup due to the stabilizing effect of the liquid viscosity. Lastly, the Re is the ratio of the inertial forces to viscous forces utilizing the relative velocities.

Several breakup models, providing the onset and total time for breakup, and the child droplet size distribution have been proposed in previous works. These models are based on both experimental measurements (Theofanous and Li, 2008; Hsiang and Faeth, 1992) and, more recently, high resolution simulations (Meng and Colonius, 2018). They have considered a wider range of initial *We*, covering various breakup regimes. A recent review of the breakup literature is given by Guildenbecher et al. (2009), and experimental and visualization tools for the different We regimes by Theofanous and Li (2008). While droplets in our experiments will undergo a breakup process, we emphasize that the focus of this paper is on the evaporation of droplets, primarily after a breakup process has occurred.

The following sections present the existing experimental facility for creating the SDMI, the new experimental equipment and calibration procedures for measuring acetone droplet vapor concentrations, the image processing techniques applied, and a discussion of the results obtain from an evaporating SDMI experiment.

2. Experimental facility

In the following section, a description of the existing experimental facility and equipment upgrades for reliability and measurement of acetone droplets, will be detailed.

2.1. Shock tube facility

The experiments presented here were run in our shock tube facility (Fig. 1), which produces a mechanically driven shock wave using compressed gas. The shock tube is closed-ended and horizontally-oriented (i.e., parallel to the floor) to observe the development of a cylindrical multiphase interfaces morphology during the experiment. The shock tube is comprised of three conjoined sections: (1) the driver section, responsible for storing highpressure gas to initiate and sustain the shock wave, (2) the driven section, which allows the shock wave time to fully develop, and (3) the test section where the shock wave interacts with the interface and the resulting morphological development is imaged. The driven section is a round tube made of steel with a ~ 22 cm inside diameter and length of ~ 150 cm. The shock tubes driven, and test sections are both square tubing made from cold-rolled steel, each with a cross-section of \sim 15.4 x 15.4 cm. The three sections together have a total of ~ 9.5 m in length. The driver and driven sections are separated by a thin (0.030 in for this work) acrylic diaphragm that may be ruptured rapidly. Once the diaphragm is ruptured, it expels the compressed gas from the driver section into the driven section, which is initially at atmospheric pressure. An "X-shaped" knife edge rests just below the diaphragm (on the driven section side), to cut the diaphragm uniformly as it breaks resulting in a more repeatable rupture pressure. The required commercial, off-the-shelf equipment for diagnostics and data acquisition, as well as the custom apparatuses developed to generate the droplets, are located in the test section. Additional details on the shock tube facility are provided by Middlebrooks et al. (2018).

The shock waves velocity and pressure are recorded by two dynamic pressure transducers (DPT) located at the end of the driven section prior to the test section. The pressure measurements taken from the two DPTs are utilized to precisely trigger the timing sequence for our cameras and laser and to calculate the shock wave's strength. This enables us to accurately capture images of the multiphase interface at predefined times during the interfaces development. As the interface develops, it propagates through the test section. To image the interface development at specific times in its development, the test section hosts multiple windows shown in Fig. 4 that provide optical access at specific locations for capturing the resulting interface. The software LabVIEWcontrols and executes the automatic shock firing sequence and communicates with TSIs Insight 4G This software is used to control the precise timing of the laser illumination and camera exposure to capture interface development images. The laser is a Litron Nd:YAG NanoPIVlaser. The NanoPIV is a dual head laser that provides 200 mJ and 40 mJ of laser energy at 532 nm and 266 nm wavelengths, respec-

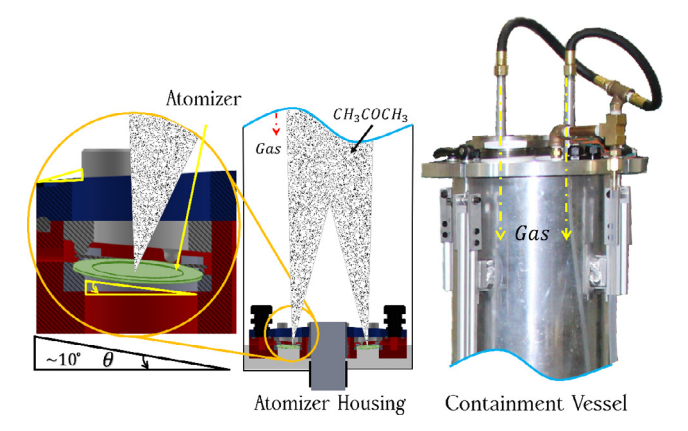


Fig. 2. Droplet generation apparatus.

tively. The CCD cameras used to acquire images are a 4 MP camera for capturing the particle field (scattered 532 nm light in the visible spectrum), and a 29 MP camera for capturing gaseous acetone fluorescence ($\sim 350-550$ broad-spectrum light). Each camera captures a set of two sequential images (i.e., image frames A & B) for each set of experimental or calibration data collected. Additional information on the experimental controls and data acquisition can be found in Middlebrooks et al. (2018).

To further improve the reliability and uniformity of droplets compared to our previous devices (Middlebrooks et al., 2018), we developed a new droplet generation apparatus (DGA, see Fig. 2). This improved apparatus enables the use of liquid acetone (instead of just water as was used before), which degrades many materials utilized by our previous design. The DGA itself is comprised of a containment vessel (an exterior shell) and the atomizer housing, which holds the atomizer devices and generates acetone droplets within the vessel. The new containment vessel was constructed from a 6061-T6 aluminum tube with enclosed ends. Within the vessel, new liquid atomizers were mounted inside the atomizer housing to generate and mix liquid droplets with the carrier gas. The vessels top has two viewports (windows) for visualization of the atomizers. It has two inlet ports for gas flow and enables better mixing of the droplets and gas. The vessel uses a pressure relief valve system to prevent over-pressurization from the momentary post-shock pressures. Further, it uses a system to monitor and maintain the vessel's liquid level at the proper amount for the atomizers to function.

The vessel also has a removable lid secured with four clamping cam handles and sealed by a polytetrafluoroethylene (PTFE) Oring to prevent any flow losses (i.e., leaks). The mixed fluid flows through a gradual reduction pipe fitting (2 *in* NPT to 3/4 *in* NPT) with a total length of ~ 32 cm, to ensure a smooth, laminar, fully-developed flow profile before entering the shock tubes test section. Lastly, this pipe reducer fitting is also used to mount the atomizer housing inside the vessel, keeping the atomizers at a precise height to the liquid surface. The specifics on how the atomizer housing generates acetone droplets are discussed in the following section.

2.2. Droplet creation equipment

To generate liquid acetone droplets, eight metal mesh piezoelectric atomizer transducers are affixed inside the atomizer housing. The transducers generate droplets highly uniform in size from an acetone bath below by passing the liquid through micro-sized holes in a metal mesh resonating at a frequency of 100 kHz. To properly generate droplets, the transducers must be mounted with minimum damping, such that they can resonate properly inside the atomizer housing. So that, they will be mounted at a precise



Fig. 3. Filtration retention device.

location with respect to the liquid surface below them. If the transducers are mounted too high, they will be unable to pump to liquid efficiently. If they are too low, the liquid may prevent them from oscillating correctly. To achieve these requirements, a rigid cylindrical mounting device (i.e., the atomizer housing) situates the atomizers precisely at the desired fluid level. The atomizer housing, made of 6061 aluminum, is composed of three main pieces: (1) a circular bottom plate to house the atomizers and wiring cables (2) a top plate with a ten-degree slope away from the central axis to shed excess fluid buildup from fallen droplets collecting on top, and (3) eight rigid atomizer mounting fixtures affixed in between the top and bottom plate plates. The top and bottom plates are sealed together with two PTFE O-rings to form an internal dry cavity for running wiring to the atomizers. Each insert is designed to hold one atomizer transducer, 30 mm in diameter, at a ten-degree angle to shed excess liquid buildup on its top surface from settling droplets.

The atomizing transducers utilized are unfortunately not chemically resistant to acetone. To mitigate this issue, we coated the transducers piezo material (an outer ring on the transducer) with a layer of silicone to protect the vulnerable factory epoxy adhesive layer, prolonging the device's operation and functionality in the harsh acetone environment. Additionally, each atomizer was re-soldered with chemically resistant electrical wires. By doing so, each atomizer is protected and externally controlled to produce the desired particle droplet output for the experiment. Specific to this experiment, two high output atomizing transducers were utilized to create droplets with a mean droplet diameter of 10.7 μ m at sufficient concentration to generate the desired interface A_e of ~ 0.225 .

To quantify the droplet concentration (i.e., multiphase interfaces A_{e}) entering the shock tube test section, a new custom filtration retention device (FRD) was built, as shown in Fig. 3. The FRD filters particles that are above a prescribed diameter out from the gas flow, so that only particles at or below the desired maximum diameter may pass through. In addition to this, the FRD minimizes any additional back-pressure generated while collecting the sample by maximizing the filter surface area and thus replicating the mixtures flow rate during experiments. The mass of the retained particles can then be weighed and compared with the measured gas mass flow rates to determine the resulting effective density, ρ_e , of the multiphase particle-gas mixture for the initial conditions. The retained fluid is weighed with a digital precision balance scale, 0-300 g range, with an accuracy of 1 mg. Acquiring data on the resulting effective density mandates makes the measurement conditions as close to those of experiments as possible. This is achieved by measuring the effective density via placing the FRD at the same location as the mixture would otherwise enter the shock tube test

The FRD components are 3-D printed and coated with a layer of silicone to prevent undesirable acetone interactions. The top and bottom FRD components are comprised of two pieces used to

clamp the filtration paper into place. A water-tight seal is achieved between the two pieces and the filtration paper by applying a thin layer of silicone. Multiple FRDs were manufactured and tested to allow quick repetitive measurements of the effective density. For this work, the filtration paper used was made of a Nylon membrane and PET substrate with a pore size of 5 μ m (effective for capturing nearly all droplets generated by the atomizers with a mean size of 10.7 μ m).

To precisely calibrate the experimental equipment for acetone vapor imaging, we designed and developed the calibration frame apparatus (CFA). The CFA is utilized to create a small volume of acetone vapor at precise constant temperature and pressure for measuring the acetone fluorescence signal at different locations within the experimental apparatus and laser field. This measurement is then used to calibrate the fluorescence measured in experiments to the local conditions of the experiment and laser sheet. The CFA is manufactured from nylon powder due to its chemical resistance to acetone. Its design allows it to be positioned at any location in the laser sheet's path in which images of the SDMI are taken. The CFA has two high-temperature quartz glass panels, which are used as UV transparent windows to visualize the laser sheet and reduce light backscattering effects. Additionally, two borosilicate glass windows offer optical access for the cameras to acquire images of the acetone field. All UV and borosilicate optical viewport windows are sealed with silicone to ensure an airtight seal. The gas is filled from the top and exhausted from the bottom without contaminating the inside of the shock tube. Lastly, the CFAs base is affixed with magnets such that once aligned with the mid-plane of the shock tube; it remains tamper-resistant and stationary.

These newly-developed experimental apparatuses each enable acquiring sets of more consistent and reliable experimental data and work in harmony with the previous shock tube equipment and design. Their descriptions and utilization techniques are provided next within the experimental methods section.

3. Experimental methods

The following sections present the methodologies and required procedures followed throughout the experimental setup and Q-PLIF calibration process. The procedures must be methodically executed to ensure a high level of reliability in the results. Many experimentalists well know that the acquisition of accurate Q-PLIF images is difficult and requires a high degree of repeatability and control. To further complicate this, the imaging equipment is quite sensitive to its position relative to the shock tube and imaging plane. For instance, cameras are moved to different windows in the shock tube to image the interface at different development times; so, even the slightest deviation in position or adjustment could result in increased light contamination and decreased optics performance. Thus, to maintain a high level of confidence in our data, it must be collected within a short time (within the workday) of each calibration process.

3.1. Laser alignment and calibration

Prior to each experiment, the laser and optics' alignment must be verified, and the optical equipment cleaned to guarantee appropriate performance during the experiments. The first step in this procedure is to confirm that the lasers beam output is aligned concentrically to the shock tube's centerline. Then, the laser heads are each aligned in the near-field and far-field using a calibration target; so that both heads beam output converges to a singular point. After both laser heads are calibrated, the focus of the cameras may be held constant from experiment-to-experiment, as the location of the image plane does not change. With each of the

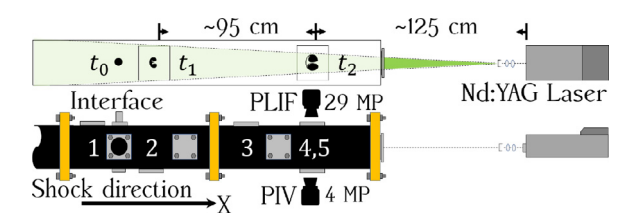


Fig. 4. Laser divergence and locations of the experimental images.

laser heads aligned, the external optical components (e.g., lenses) are then aligned and calibrated. To do so, plano-convex and plano-concave spherical lenses are positioned to focus the laser beam to a concentrated point. The beam is then diverged into a sheet using a plano concave cylindrical lens. The beams output is a sheet less than 1 mm thick to illuminate the interface along the *xy* plane.

After performing the laser system alignment procedure, focusing and aligning the cameras is performed. Each camera is affixed perpendicularly to a specific shock tube window. The interface development time to be imaged dictates which set of optical viewport windows the cameras are affixed to. A representation of the viewport window locations is shown in Fig. 4. The 29 MP camera is used to image the acetone vapor fluorescence with a lens aperture of f1.2. A UV transparent fused silica filter is affixed to the lens to remove all reflected light from the 532 nm (\pm 1 nm) laser emissions. Images of the particle flow-field are captured by a 4 MP CCD camera with a lens aperture of f4. The camera is filtered by a narrow band-pass filter such that any wavelength of light outside of 532 \pm 2 nm is not transmitted to the CCD cameras image sensor. Neutral density filters are mounted to the 4 MP camera to lessen the intensity of reflected laser light when capturing the particles' images within the flow-field. This allows the lens aperture to be smaller and the depth of field to be narrower, producing sharper images. To allow a wider field-of-view for both cameras, close-up, diopter lenses are also utilized to obtain the maximum field-ofview possible without diminishing resolution or resulting in partial image (data) loss.

After the laser, its external optics, and the cameras have been aligned; each camera must acquire calibration images which consists of the following information: (1) a background (noise) calibration image, (2) a total flow-field size calibration image, and (3) a frame-to-frame image intensity variation calibration image while using the CFA. Because the morphology of the interface is captured at multiple locations (see Fig. 4), these standardizations must be performed at each location to ensure reliable experimental data is collected. Size calibration images are necessary such that the particle image taken by the 4 MP camera and the gas image taken by the 29 MP camera may be properly overlaid on top of one another; that is to say, pixels-per-millimeters ppmm homogeneity is achieved. To calibrate for variation in ppmm between the two cameras, each camera is focused and acquires an image of transparent paper (3.175 mm x 3.175 mm x 0.1 mm) embedded with an opaque grid whose location is coincident with that of the laser sheet. Focusing is executed such that the optimal resolution of the grid is ascertained; assuming effects from the paper thickness are negligible. An example of a size calibration image is illustrated in Fig. 5. A finer adjustment of the camera focus is performed using a heterogeneous (steep gradients present) sample of interface fluid (droplets and vapor) to focus on the droplets and vapor field more precisely. Background calibration images (i.e. dark frame and light frame noise calibration) are taken to account for spurious background noise, which could contaminate the experimental image data due to the variations in the cameras operating temperature as well as light pollution (e.g., undesirable internal light reflections within the shock tube). The final set of calibration images

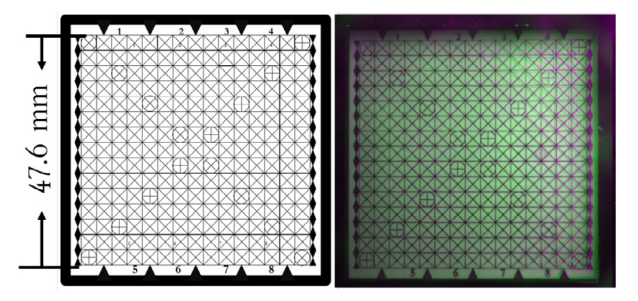


Fig. 5. Overlaid size calibration image of the 29 MP and 4 MP cameras.

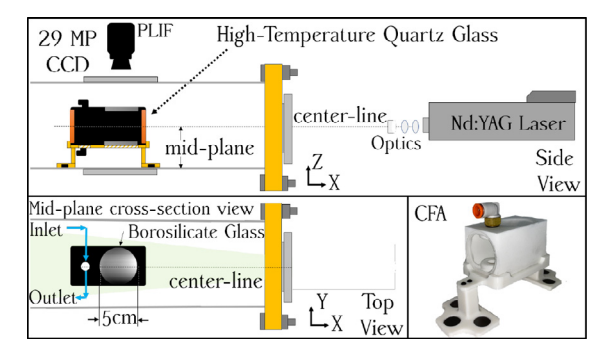


Fig. 6. Acetone calibration frame apparatus.

obtained using the CFA enables correcting for span-wise variation, laser head variation (LHV), laser location variations (LLV), and attenuation of the signal. A more detailed description of how these images are processed is discussed in Section 4.

At least four background, flow-field, and frame calibration images are captured before performing any SDMI experiments. When performing the calibration procedure, the camera exposure is kept constant with the SDMI experiment. Specifically, for the frame calibration, each frame provides a spatial map of the light sheet, laser intensity, and laser profile for the calibration frame images based on its location. To measure differences in these quantities, the CFA is filled with nitrogen saturated with acetone vapor. Once the cell is uniformly filled with the mixture, images are captured for both laser heads at each camera location. For imaging, the calibration frame shown in Fig. 6 is oriented such that the laser light enters and exits in the quartz glass windows.

3.2. Interface characterization

Now that the specifics of the newly-developed custom FRD apparatus have been provided, the methodology for using it to characterize the multiphase flows properties is presented. To generate the interface itself, the following procedure is followed. Nitrogen gas is flowed into the acetone seeder, which saturates the nitrogen with acetone vapor. Acetone is evaporated from a liquid acetone bath within the seeder where the liquid temperature is held constant using an internal heater (i.e., resistance heating element). The temperature of the liquid is measured with a thermocouple where a feedback loop regulates the power to the heating element to achieve the desired constant temperature (room temperature ~ 20°C). The now acetone-vapor-saturated nitrogen gas mixture enters the DGA's vessel, where it mixes with liquid acetone droplets, generated by the transducers within the atomizer housing. For this work, atomizers with a mean droplet diameter of 10.7 µm were used. The manufacturers specifications regarding the mean acetone droplet diameter and distribution per transducer have been verified against the particle interferometry technique; for further details see Kothakapa (2017), and Middlebrooks et al. (2018).

The FRD measures the multiphase mixture (acetone aerosol) entering the shock tube's test section, which is comprised of: (1) Nitrogen gas, (2) acetone vapor, and (3) liquid acetone droplets. To measure the quantity of droplets, samples of the interfaces droplet flow are collected by the FRD for one or two minutes, in this case at a nitrogen flow rate of 3.4 SLM (the experimental condition). The droplets collected are then weighed multiple times using our precision balance. By taking many repeated samples, a greater understanding of the interface particle concentration statistical behavior is achieved. This, of course, is the concentration of interface prior to being whitg by the shock wave. From the FRDs collected samples and psychometric theory, the concentration of the sample can be determined. The multiphase mixture is taken to be at psychrometric equilibrium and therefore saturated with acetone vapor. The pressure NIS (2020) of the acetone is then calculated using the Antoine equation (valid in between 259.16 - 507.60 K), $log_{10}(P) = A - (B/(T+C))$, in which P is the vapor pressure bar, T is the temperature in K, and constant values A, B, and C are equal to 4.424, 1312.253, and -32.445 respectively. Knowing the time over which each sample is acquired in addition to the dry gas mass flow rate, the nitrogen mass can be calculated for the mixture. From the psychrometric mass fraction of the mixture occupied by each gas component at saturation, the mass of acetone vapor is calculated. The mass contribution of liquid droplets is obtained from the weight of the FRD samples collected. Once each of these pieces of information is gathered, the mass concentration can be determined. Then, from the total mass and volume occupied by the samples, the effective density can be calculated. The mass concentration of each of the different constituents of the mixture was calculated to be 45 % / 31 %/ 24 % for nitrogen, acetone vapor, and acetone liquid droplets, respectively. With the effective density of the interface now determined, the effective Atwood number, A_e , can be computed.

Calculation of the effective Atwood number provides insight into the density gradients effect, and the upper limit for the strength of the SDMI. The effective Atwood number for the previously described mass concentration values was found to be $A_e \sim 0.225$, (see Section 1). Now, the initial fluid properties for the experiment have been quantified. A series of SDMI experiments may be run now to observe the interface's behavior at two times after shock acceleration, at an upstream (less developed flow) and downstream (more developed flow) location.

3.3. Experimental procedure & data collection

Up to this point, the experimental equipment has been calibrated and the interface has been characterized; thus the stage has been set to instigate the SDMI. This is achieved by initiating the automatic shock firing sequence (ASFS) within the authordeveloped LabVIEW VI program. The ASFS is started when the driver begins to fill with high-pressure gas. The ASFS enables the automated control of all the experiments equipment (e.g., cameras, laser, DPT, mass flow rates, nitrogen flow control valves, and interface mixture generating apparatuses) by preset driver pressure thresholds, or conditional ætriggers,g to control the equipments operational states or outputs. Within the ASFS, there are three stages initiated by the driver pressure thresholds: (1) At the beginning of the sequence droplets are created in the DGA for about 35-40 s) before the shock wave hits the interface. During this time dry gas is continuously flowed into the shock tube from the upstream and downstream locations. (2) The gas mass flow controllers are activated, flowing the mixture of nitrogen and acetone droplets and vapor into the tube and creating an interface. At this time, the data acquisition system is started (i.e., laser signal, Insight 4G, and camera sensors). (3) Finally, an additional amount of gas is rapidly added to the driver by a fast acting valve, causing a nearlyinstantaneous rupturing of the diaphragm and releasing the driver gas into the driven section. This additional gas (nitrogen) is released in a short-timed burst from a reservoir tank at 500 psi. The compressed-gas, now traveling from the driver to the driven section, produces a normal shock wave with a jump in the velocity of $\sim 300 m/s$, and a post-shock pressure, and temperature of $\sim 305 kPa$ and $\sim 412 K$ respectively from ambient conditions.

Prior to reaching the test section, the driven sections DPTs are triggered by the shock wave's increased pressure, which then triggers the laser imaging timing sequence and thus captures images of the SDMIs development. The DPT data is used to measure the shock wave velocity to be $\sim 575m/s$. Part of the laser imaging timing sequence includes triggering the lasers synchronizer, which fires two laser pulses separated by 2 µs (appropriate for PIV measurements) and sequentially initiates the CCD camera sensors (digital shutters). Once the sensors are activated, images of the SD-MIs development and morphology are captured by each camera in their respective frames (i.e., frame A & B). A visual representation of the experiment is provided in Fig. 1. This procedure is repeated for each experimental trial and the camera calibration procedure is performed each time the cameras are moved to a different window location (two locations are used). Once each camera has captured both sequential image frames, the images are then processed.

4. Image processing methods

A detailed explanation of our image processing techniques is presented in this section for correcting the images obtained during the calibration and experimental phases of this research. It is worth mentioning that image processing should be meticulously performed as not to alter the data collected. With this in mind, Q-PLIF images are processed to produce accurate fully-corrected images, whereas PIV images are processed to quantify the flow velocities.

4.1. Background noise correction

The first step of the image processing method is to subtract the background signal. Background calibration (i.e., subtraction) is done to reduce noise in the images of the experiment brought on by outside sources such as ambient light in the FMSTL laboratory. The image background subtraction procedure is described by the following equation, $S_{ij} = I_{ij}^{\ \ raw} - (I_{ij}^{\ \ bg})$, in which S_{ij} is the corrected intensity from an average intensity background signal from the experimental facility, $I_{ij}^{\ \ raw}$ is the intensity captured by the CCD camera, and $I_{ij}^{\ \ bg}$ is the average background intensity in the calibration image.

4.2. Divergence correction

The second image correction method takes into account variations in the flow field illumination. The laser sheets intensity both diminishes as the laser light propagates away from the laser itself, and the sheet diverges (i.e., spreads) as it propagates down the test section. It is crucial to adjust each image by accounting for the spatial variation in light intensity. In order to do so, the images are first modified to account for the divergence variations (i.e., straighten the laser path) in order to further correct for laser profile, attenuation, and index of refraction correction. This is achieved by following the procedure from Mohammad (2019) and Christopher (2012), where the intensity of the divergent plane is transformed into a straightened plane using Eq. (1).

$$S_{ij}^{trans} = S_{ij} \frac{(y_{int} - 1)}{(y_{int} - y)}$$
 (1)

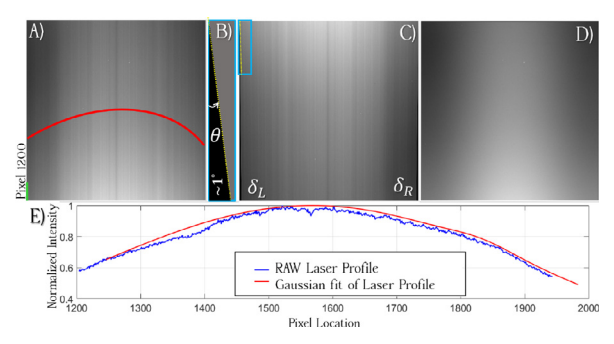


Fig. 7. Calibration image: (A) original, (B) close-up of the divergence angle, (C) laser divergence correction, (D) index of refraction correction and (E) Gaussian fit of the laser profile.

In this equation, S_{ij}^{trans} is the intensity of the images after they are straightened, y_{int} is the distance from the lasers divergent optical lens' focal point to the location (pixel) within the image, and y is the vertical distance from the top of the image itself to the images pixel location Mohammad (2019). Fortunately, the angle of divergence for our apparatus is small due to the external optics concave lens focal length being quite large (f=500 mm); a favorable condition for these experiments regarding the image correction process. Finally, to maintain the original resolution of the images post correction, the calibration and experimental images are resized by a factor $(1/(1-(\delta_L+\delta_R)))$, in which δ_R and δ_L are the distances from the right and left side of the top images for correcting the divergent plane Mohammad (2019).

After the divergence correction procedure is completed, the rays of light generated by the laser are all now straight and parallel, allowing correction for attenuation, striations, and laser profile, as shown in Fig. 7. The next image processing step accounts for the signal attenuation caused by the light traveling through the acetone interface, getting absorbed along the way and diminishing the signal intensity. Beers law governs this phenomenon. Attenuation correction was performed for the calibration images; however, this step was neglected during experimental image processing since the interface morphology is essentially too thin for significant attenuation of the laser to occur as it travels through the thin ($\sim 1-3mm$) acetone field.

4.3. Laser profile and attenuation correction

The calibration images acquired prior to experimentation using the CFA must be processed further to produce a smooth profile for correcting experimental images. Images of the acetone flow-field in the CFA are passed through a median 2-D filter to reduce spurious noise before correcting spatial variations in the lasers intensity profile and attenuation effects. A function, f(y, z), is obtained from the calibration frame using a second-order Gaussian fit to correct for attenuation in the calibration frames. Similarly, fluctuations caused by the lasers intensity profile are corrected by applying another Gaussian fit function, f(v, x), that corrects for the loss in signal due to the decrease in laser intensity away from the center-line. Consequently, the row-by-row function, f(y, x), is applied to the calibration images and experimental images from their corresponding frame and image location. A graphical representation of this procedure is shown in Fig. 8 and 9 for the calibration images, and in Fig. 10 for the experimental images.

4.4. Index of refraction correction

Striations in Q-PLIF images occur whenever a laser refracts through a mixing interface (complex morphology) with different optical properties. As the flow becomes more turbulent, a higher

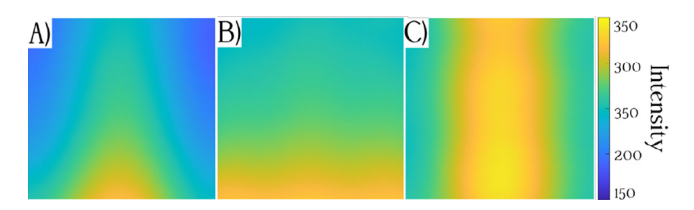


Fig. 8. Correction in (A) the original calibration image due to: (B) laser profile, and (C) attenuation.

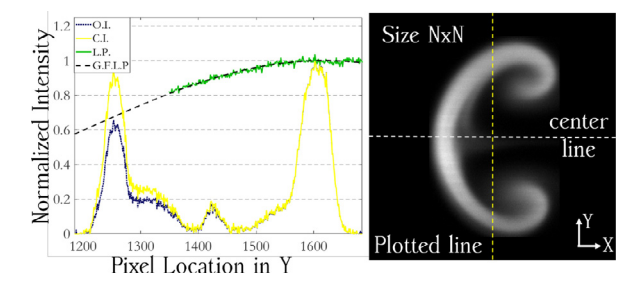


Fig. 9. Example of the laser profile correction for an image. Right: The corrected PLIF image taken at $500\mu s$. The vertical dashed yellow line shows the location of the example data presented in the intensity graph to the left. Left: Graph of the laser intensity correction and image correction applied along an example 1D slice of data (dashed yellow at right). Green line: Raw laser profile (L.P.) data. Dashed black line: Gaussian fit of laser profile (G.F.L.P.). Blue line: Original intensity (O.I.) profile of experimental image. Yellow line: corrected intensity (C.I.) of the experimental image. (For interpretation of the references to colour in this figure legend, the reader is referred to the web version of this article.)

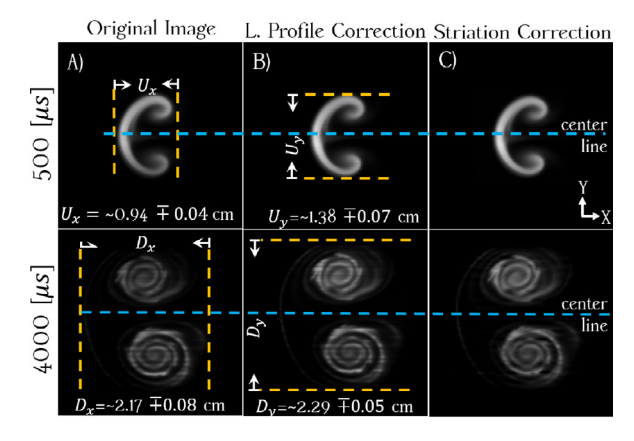


Fig. 10. SDMI interface and mixing widths at 500 and 4000 μs .

number of striations are observed, increasing the complexity of the correction method. These streaks are challenging to correct in the spatial domain because of their non-periodicity and the complex contours in the experimental images. As a result, they were corrected utilizing functions in the frequency domain (2D-Fourier Transform), where they are all grouped together on a horizontal line.

Before the striations can be corrected, the experimental and calibration images must first be calibrated using the previously described methods. Then a region of interest (ROI) is selected in which the correction will be applied. The ROI is obtained for the experimental images and applied to the calibration images with a built-in algorithm that outputs a gradient selection of the experimental image of size ($N_{\rm max} \times M_{\rm max}$), and modifies it to obtain a square region of size ($N_{\rm col}$) from the center of the interfaces morphology. The size of $N_{\rm col}$ calculated from the gradient selection, can be adjusted to further allow for an increase in the transformed image frequency domain. Once the ROI is selected from the experimental images, background, divergence and a Gaussian fit

laser profile, corrections are applied. The fidelity of this method is shown in Fig. 9. From the experimental centerline and the calibration profile, Fig. 9 shows the corresponding normalized intensity of the experimental image at the same location as the calibration frame. After applying the Gaussian fit of the laser profile, it can be seen that the left sides of the experimental images were corrected while the right sides remain unaltered, resulting in a more balanced representation of the multiphase flow.

Once these simpler corrections are applied, we proceed to correct the images for the vertical striations due to the laser refraction. The square ROI from the experimental image is zero-padded and mirrored from the center of the images on all sides to create a periodic array of intensity values (Mohammad (2019), Christopher (2012)). The result is a mirror image of size (3Nx3N), replicating the spectrum frequency to amplify the frequency and reduce the loss of the image's resolution. A twodimensional Fourier spectrum analysis provides an equivalent representation of the spatial domain into the frequency domain where wavenumbers $(k_i \text{ and } k_i)$ are given in the i and j directions with respective amplitudes $A_{i,j}$ at each i, j location. The reference point of the frequency domain is shifted from $(0 - 2\pi)$ to $(-\pi - \pi)$, resulting in a group of low-frequency clusters at the center of the image, and high-frequency modes at the edges. In the shifted frequency domain, all vertical streak discontinuities are located at $k_i = 0$.

A notch filter mask is applied at $k_i = 0$ to remove the spectral band, excluding the region close to the center. The removed components are replaced with interpolated values. The interpolated values are taken from a two-dimensional radial spectrum outside the notch filter mask (average of all values for which $|\mathbf{k}| = k_i$ where k_i is the value in the notch filter to be replaced); a similar procedure follows in Christopher (2012). An iterative approach is followed in order to obtain the best mask-fit for the experimental and calibration frame images. The mask-fit varies the point from the center, height, width, and the radial pixel region of the mask in order to converge on the best image representation. Finally, the striation corrected images are obtained by transforming the image back to the spatial domain using the inverse Fourier transform, cropping the mirrored portions of the image, and scaling the image to its original size by reversing the padding of the image. The final size of the corrected images is equivalent to the original (NxN). This Fourier notch Itering procedure is used to process all experimental (see Fig. 10C) and calibration images (see Fig. 7D).

4.5. Frame-to-Frame image calibration

Once all experimental and calibration images are corrected, the images are next calibrated for the laser location variations (LLV) as a function of location in the shock tube, and laser head variation (LHV) due to different energy outputs the laser's beam. This correction is done using the calibration images. Since the calibration images are taken for uniform and identical acetone conditions in the CFA, a map can be developed to normalize the acetone fluorescence signal at each location to one another. This map can then be applied to the experimental images as well. To do so, frame A (downstream) will be taken as a reference calibration point to normalize the other locations and frames. Thus, frame B (downstream) will be normalized for the laser head variation to correspond to frame A (downstream). Once the downstream frame is adjusted, we proceed to correct frames A & B upstream. The frame B (upstream) is normalized first for the LHV to be equal to frame A (upstream). Lastly, both upstream frames are normalized to frame A (downstream) to account for the LLV. With this procedure executed, all image intensities are now independent of their location and laser head variations.

4.6. PIV Processing

All PIV images presented in this work are obtained with the 4 MP camera. Before the PIV software is run on the image pair, the images are pre-processed. The first step is to select a rectangular ROI from the images, which captures the full interface morphology. The image contrast is then enhanced with limited adaptive histogram equalization, enhancing the zones of high intensity and lowering the exposure of other regions. A Wiener filter was applied to improve the particle signals and reduce the effect of random noise in the experimental images. Once the image pre-processing is completed, the PIV analysis of the images is performed using a fast Fourier transform (FFT) algorithm. Evaluating all the other methods (i.e., direct cross-correlation (DCC), ensemble correlation (EC), and FFT) provided by PIVLab, it was found that all of them provide similar results. The FFT algorithm was chosen because it offered a refined solution after utilizing multiple interrogation areas; hence minimizing the loss of information, providing an optimal signal to noise ratio.

The FFT window allows for the adjustment of the pixel spacing to identify the particles when moving from one location to another. The grid spacing has three square regions decreasing in size, 128x128 px for the first pass, 64x64 px for the second, and 32x32 px for the third. Once the particles are tracked, a 9-point fit (2D Gaussian fit) is performed to provide interpolated data points from the particles and increase the displacement estimation accuracy Thielicke and Stamhuis (2014). The two experimental images are calibrated in size and with a time of 2 μs between images to provide velocities in m/s. Finally, vector validation is performed using the region of high-velocity vectors by rejecting vectors outside a lower and upper threshold, determined from the image statistics. Statistics of the particle motion are obtained after subtracting the mean velocity in both directions. Results are smoothed and processed through a median filter to reduce the influence of noise and highlight the flow phenomena. Circulation is calculated by the integral line method, where circulation is defined as the line integral around the closed contour of the velocity components locally tangent to the contour (Eq.. 2). A series of thirty circles that evenly increase in size, from the center of the vortex, is used for the contours. The tangential velocity vectors are approximated and calculated on the circles to obtain the circulation until the maximal circulation is found.

$$\Gamma = \oint u \cdot dl \tag{2}$$

By overlaying the PIV results gathered from the acetone droplets with the acetone vapor field, a complete view of both the large and small scale mixing can be obtained. The overlay is accomplished by taking four coordinate points (x,y) in the 4 MP (2352x1768) and 29 MP (3296x2200) cameras and mapping them together. A scaling factor is found for the coordinate points to shrink or expand the images. After the 4 MP calibration image is scaled and shifted to match the 29 MP image's location, the 29 MP image is flipped to maintain the same direction of the flow pattern.

5. Results

5.1. Interface evolution and morphology

The interface evolution is driven by the formation of two strong counter-rotating vortices. As the shock travels through the circular interface, it crosses into and out of the multiphase fluid, primarily interacting with both an upstream and downstream interface. It deposits the strongest vorticity, similar to the RMI, where the misalignment between the effective density gradient and pressure gradient is highest, the top and bottom-most points of the circular interface. These points mark the centers of the two counter-rotating

vortices. The interface is initially compressed in the x-direction by the shock wave before it begins to grow again. As the primary vortices evolve, they develop secondary vortices along with the swirling gas interfaces, mixing the multiphase mixture with the surrounding clean gas. Eventually, the interface will evolve into a state of decaying turbulent mixing.

To quantitatively compare the interface morphological evolution, all experimental images have been converted from px to cm with the size calibration image. A basic measure of the interface mixing can be made using the interface mixing width, borrowed from previous RMI work. A growing mixing width implies that the interface is growing and mixing with the surrounding clean gas. The mixing width represents the distance between the edges of the interface. Here, we use both the distance between edges in the x (shock direction) and y-directions. Initially, the interface width is 12.5 mm in diameter. At 500 μs , the interface has decreased 28 % in the x-direction, due to the shock compression, and increased 11 % in the y-direction, see Fig. 10A & B upstream. As the interface morphology evolves and grows, the mixing width increases. At 4000 µs the interface width has increased by 84 % in y-direction and 66 % in x-direction, see Fig. 10A & B downstream. Secondary vortices can be seen forming on the primary roll-ups, as the flow mixes and evolves towards a state of decaying turbulent mixing.

While the interface is initially saturated with acetone vapor after the shock passes, the carrier gas temperature increases along with the acetone saturation pressure, and the acetone droplets begin to evaporate. Locally, the mass in the system must be conserved as droplets evaporate, so during phase change, the mass of the liquid acetone transfers to mass in the vapor phase. This additional vapor mass increases the intensity of the acetone fluorescence signal captured by the CCD camera. The increase in signal intensity will continue until the droplets evaporate entirely. The rate of evaporation is dependent on the gas temperature and large-scale mixing (i.e., circulation). The gas temperature is a problematic metric to determine as it cannot be directly measured with our current techniques independent of acetone concentration. However, it is known that the bounds must be between the preshock (~ 293 K) and post-shock (~ 412 K) ideal-gas temperatures. It was previously shown via simulations from Paudel et al. Paudel et al. (2018) that the interface gas temperature, for similar shock conditions with water droplets, is maintained at the wetbulb temperature. This finding is supported by approximating the system as constant pressure, two-phase, thermodynamic system. Using psychrometric equations, the post-shock acetone wet-bulb temperature is estimated to be at ~ 325.5 K. We take this to be the gas temperature after the flow reaches a steady evaporation state, very early in its evolution (< 100 µs, determined from theoretical evaporation rate).

5.2. Velocity and vorticity

To continue the interface evolution discussion, we turn to the PIV results to show the interface features' velocity and the strength of the primary vortices driving the interface evolution. The velocity is acquired directly from the software analysis of the two PIV image frames, and the vorticity is calculated using a first-order finite difference approximation.

After the shock passes through the unperturbed interface, the gas behind the shock experiences a velocity jump of ~ 300 m/s (piston velocity from 1D gas dynamics and post-shock conditions describe in sec 3.3). With this in mind, at 4000 μs the interface has a mean velocity in x of $u_x = 276.57 \pm 7.64 \frac{m}{s}$, relatively similar to the calculated piston velocity. The mean velocity and standard deviation are calculated as the mean of all velocities and standard deviation values within the samples. After subtracting both mean velocities, the magnitudes of the resultant vectors are plot-

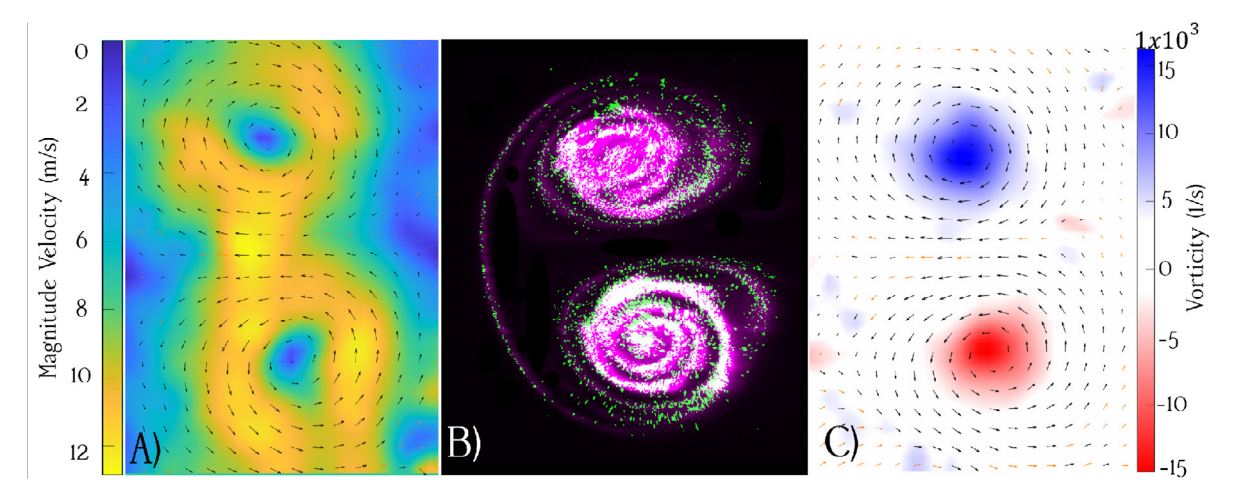


Fig. 11. SDMI interface at $t \sim 4000 \mu s$: (A) Magnitude of the velocity field, (B) Overlaid images of the gas and particle field, and (C) Vorticity field.

ted in Fig. 11A. From the overlaid images in Fig. 11B, significant evaporation of the droplets has occurred, but they have not vanished completely.

At this specific time, (i.e., 4000 µs) shown in Fig. 11B, the droplet, and gas flow fields' dynamics align well. This indicates that the droplets have equilibrated in velocity with the gas. In fact, this can be shown with the particles Stokes number (St), which was calculated to be close to or less than 0.1, following the method used for the SDMI in McFarland et al. McFarland et al. (2016). Given this, the droplets should be nearly in velocity equilibrium with the gas and able to follow the small velocity fluctuation in the flow. Both the theoretical velocity equilibration time (note that evaporating droplets should equilibrate faster than this time due to their decreasing size) and previous simulations support that the droplets and gas should reach velocity equilibrium early in the development, on the order of 100µs after shock acceleration. At this late time, both the gas and droplets are in thermal and phase quasi-equilibrium as well, staying at the estimated wet-bulb temperature at ~ 325.5 *K*.

Fig. 11 C shows two strong vortex cores that are produced after the initial shock-acceleration, driving the interface to evolve and mix with the surrounding clean gas. These vortex cores possess vorticity of equivalent magnitude but opposite in direction. The circulation (a macroscopic measurement of rotation throughout the entirety of a specific area within the flow) is computed as given in Eq. (2). The maximum circulation magnitude found for both the positively- and negatively-oriented vortices is found for a closed path around the vortex cores. The average values of positively-oriented and negatively-oriented vortex cores are $0.34 \pm 0.03 m/s$ and $0.36 \pm 0.02 m/s$, respectively at 4000 µs. The circulation taken for each vortex core is nearly equal in magnitude, highlighting the symmetry of the interface, and indicating that the initial conditions followed a nearly ideal shock-cylinder interaction.

5.3. Acetone droplet evaporation

From the corrected fluorescence images, an estimation of the vapor mass can be made. The calibration images made using the CFA at atmospheric conditions provide a point of reference for acetone concentration to fluorescence intensity. Taking that the fluorescence signal is primarily a function of pressure, temperature, and acetone vapor concentration, the experimental images of fluorescence can be calibrated for the post-shock pressure and temperature from initial conditions to provide an appropriate measure of the acetone density.

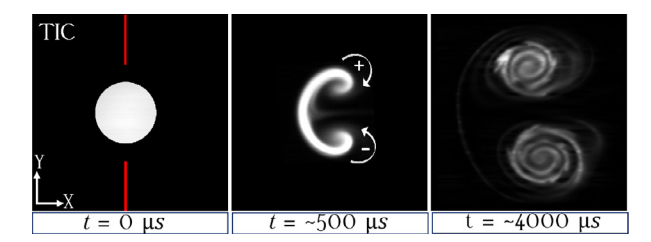


Fig. 12. SDMI interface evolution at key times. The red line indicates the position of the shock wave at $t=0\mu s$. The images are scaled in brightness so that the intensity is proportional to the acetone vapor density. The left image is the theoretical initial condition described in sec. 5.3. (For interpretation of the references to colour in this figure legend, the reader is referred to the web version of this article.)

To start, a theoretical initial condition (TIC) image is made by taking a 12.5 mm circular region (the experimentally measured diameter of the initial interface) of the corrected calibration image frame A upstream see Fig. 12. The intensity of the TIC is then scaled to the post-shock pressure and temperature to create a theoretical intensity of the initial interface acetone vapor concentration at post-shock conditions. The post-shock wet-bulb temperature is used for all subsequent experimental images as they are taken once psychrometric equilibrium is reached (steady-state evaporation is occurring). From Thurber Thurber, (1999), the correction for the variation in temperature of the absorption coefficient, $\sigma(T)$, and variation in pressure and temperature of the quantum yield, $\phi(T, P)$, is calculated. Due to the jump in temperature, the intensity signal of the theoretical initial interface must be adjusted from 290 K to 325.5 K and pressure from 100 kPa to 305 kPa, $\sigma(T) = 1.04$ and $\phi(T, P) = 1.27$ respectively. As the initial acetone vapor concentration is known from psychrometric calculations at the pre-shock conditions, the TIC image now provides a calibration value for intensity to acetone vapor density at post-shock conditions. All corrected post-shock experimental images may now be compared in intensity to ascertain the acetone vapor concentration field and the total amount of acetone vapor present. A summary of the average calibrated image intensity and estimated acetone vapor concentration at each time is shown in Table 1. Fig. 13 shows the individual measurements for acetone concentration versus time for each trial. It should be noted that due to a misalignment in the laser heads at the downstream location, the frame B downstream images were scaled to the mean intensity of frame A. This results in some loss of statistical certainty for the average acetone vapor concentration at this time (location).

Table 1 Evaporation data.

Time	Original Intensity	Corrected Intensity	Mass Conc. (mg/L)	Droplet Evap.(%)
0	2.10e7	5.26e7	71.97	0
500	2.39e7	5.99e7	80.66	15.58
4000	8.60e7	8.60e7	105.14	59.48

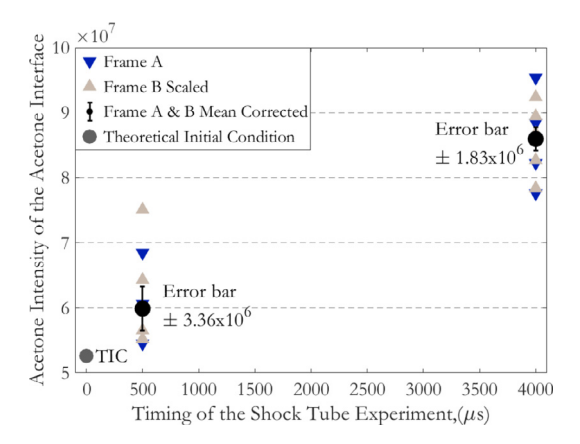


Fig. 13. Sum of the acetone intensity for each experimental image at two times in the interface evolution.

From the two locations in the shock tube, 500 μs to 4000 μs , there is an increase in average intensity of 46 %. From the initial condition interface mixture samples, see Section 3.2, the initial mass fraction of acetone corresponding to the liquid droplets and the vapor is 44 % and 56 %, respectively. From the increase in acetone concentration, we can estimate the amount of liquid mass evaporated at each experimental time. Table 1 provides an estimation of the percentage of the liquid droplet mass evaporated at the two times and shows that almost \sim 60 % of the liquid mass has evaporated by 4000 μs .

5.4. Physics of evaporation

Two different theoretical approaches are presented here to provide expected bounds for droplet evaporation rates, and to provide insight into the physics of mixing and evaporation occurring in our experiment. The first approach finds the evaporation rate of the droplets after a break-up process using the D^2 model, and constant carrier gas conditions (i.e. no mixing). The second approach is more straightforward and considers the interface a constant pressure system without mixing and reaching a psychrometric equilibrium.

First, we will discuss the breakup process for the acetone droplets. Breakup reduces the size of the droplets significantly and enhances the evaporation rate and large-scale mixing. To estimate the breakup parameters, the post-shock carrier gas conditions are required. These are estimated using 1D gas dynamics for the refraction of a shock through an interface. This estimate is somewhat complicated by the 2D nature of the interface. Simulation shows that the range of post shock values is narrow however (\pm 1%) and the 1D estimated values for velocity (\sim 290 m/s) and temperature (385K) in the air-acetone carrier gas (note these are different from the surrounding air post-shock conditions given earlier) are used here to estimate the breakup parameters (e.g. gas viscosity and density for We and Re). For a mean droplet diameter of 10.7 μ m, the droplet We is estimated to be ~ 130.5, Oh ~ 0.023, and $Re_p \sim 470.8$. For this case, the Oh is low and does not have a strong effect on the break-up process. The Re is also low compared to previous works on the breakup of droplets at a similar We. This

is due to the fact that our droplets are small ($\sim 10~\mu m$) compared to those used in these previous breakup experiments (~ 1 mm). The result is that our ratio of velocity equilibration time relative to the breakup time is approximately a factor of ten less than those considered in previous works. As the droplet's relative velocity, u_g-u_p , decreases exponentially during the equilibration process, the We will decrease significantly as breakup occurs in our case. It should be noted that this is unique from the conditions under which the previous breakup models were developed, where large droplets, on the order of 1 mm, break up well before velocity equilibrium can be achieved. For now, we rely on the previous breakup models and infer that our droplets are breaking through the sheet-stripping mechanism Pilch and Erdman (1987).

A variety of break-up models were previously explored for the SDMI by Duke-Walker et al., n.d., using simulations and experiments. It was concluded that the best data-fit for the breakup process was obtained by adapting the breakup time model of Dai and Faeth Dai and Faeth (2001) and the child droplet size model of Wert Wert (1995). This model provides a single representative size, the Sauter mean diameter (SMD), for the child droplet distribution. As the child droplet distribution is expected to be log-normal, the SMD is much greater than the majority of the child droplets. The child droplet diameter, SMD, is calculated from Eq. (3), in which d_f is the new diameter of the resulting child droplets, $\tau_{b,i}$ is the break-up initiation time, and $au_{b,t}$ the total break-up time. The parameters $\tau_{b,t}$ and $\tau_{b,i}$ are found using curve-fit equations to previous experimental data, refer to Duke-Walker et al., n.d. for more details. From the previous model, the new particle diameter is estimated to be 2.92 μm , for an initial particle diameter of 10.7 μm . The next step is to estimate the particle evaporation time for the given new particle diameter.

$$d_f = 0.49(We(\tau_{b,t} - \tau_{b,i}))^{2/3} \frac{\sigma}{v_{pg}^2 \rho_g}$$
 (3)

From energy, momentum, and mass transfer, the D^2 law establishes that the droplet diameter changes linearly with time Crowe et al. (2011). The lifetime of the droplet can be calculated from $\tau_m = D_0^2/\lambda$, where λ is the evaporation constant and is calculated using Eq. (4). In these equations D_0 is the initial droplet diameter, Sh is the Sherwood number, ρ_c is the average density at the film condition, D_{ν} is the diffusion coefficient, ρ_{p} is the material density, and $\omega_{A,s}$ and $\omega_{A,\infty}$ are the specific humidity ratios at the droplet surface and at the free stream conditions. For estimating the diffusion coefficient of acetone (A) into the air (B), we borrow from the theory of Champman and Enskog Poling et al. (2001) the equation for the diffusion coefficient, Eq. (5) (Hirschfelder et al. (1964); Poling et al. (2001)) at saturation conditions, in which T = 325.5K. In this equation T is the temperature in K, P is the pressure in bar, M_{AB} is the molecular weight of the mixture, $\sigma_{AB} = (\sigma_A + \sigma_B)/2$ is the characteristic length of the inter-molecular force law, and Ω_D is the diffusion collision integral that depends upon temperature and the inter-molecular force law between colliding molecules. Ω_D is calculated from the accurate analytical approximation of Neufield et at Neufeld et al. (1972) Eq. (6).

$$\lambda = (4Sh\rho_c D_v)/(\rho_d)(\omega_{A,s} - \omega_{A,\infty}) \tag{4}$$

Table 2 Evaporation results from the child droplet diameter.

Droplet	Initial size (μm)	Initial We	Child droplet size (μm)	D^2 evaporation time (μs)
d_1	7.7	93.9	2.1	369
d_2	10.7	130.5	2.7	588
d_3	13.7	167.0	3.2	834

$$D_{v} = \frac{0.00266T^{3/2}}{PM_{AB}^{1/2}\sigma_{AR}^{2}\Omega_{D}}$$
 (5)

From experimental results, $\sigma_A=4.6$ for acetone and $\sigma_B=3.711$ for air. At a 3 [bar]-pressure, the low-pressure assumption is valid, and there is no need for a pressure-based correction factor for the diffusion coefficient. Ω_D can be calculated from Eq. (6), where the analytical constants are A=1.06036, B=0.15610, C=0.19300, D=0.47635, E=1.03587, F=1.52996, G=1.76474, h=3.89411 and $T^*=kT/\epsilon_{AB}$. The diffusion coefficient is estimated to be $3.09e^{-6}$ m^2/s for acetone into air at the post-shock saturation conditions (wet bulb temperature 325.5 K). This value is similar to those found in other literature for acetone into air diffusion.

With this in mind, three representative sizes were taken from the initial droplet distribution to find a representative range of evaporation time for our conditions. An estimate of the initial droplet size distribution is provided in Duke-Walker et al., n.d.. While this distribution was for water droplets, the devices used were the same as this work, and it is not expected that the fluid properties have a strong effect on the droplet sizes produced by the oscillating mesh atomizers. We take the representative diameters from the representative log-normal distribution (see Duke-Walker, n.d.) at approximately the mean diameter (μ_{d_0}) , plus and minus one standard deviation ($\mu_{d_0}+\sigma_{d_0}$, $\mu_{d_0}-\sigma_{d_0}$). The D^2 model estimates that under the post-shock conditions, the evaporation rate is high enough that the droplets will completely evaporate by ~ 834 µs (for the largest initial drop size), see Table 2. However, this is not the case for our experiments, since a significant number of droplets are still observed at 4000 μ s. The D^2 model takes the free-stream gas to have constant conditions. In our case, the carrier gas is changing rapidly as it saturates with acetone vapor. Thus, the D^2 model over predicts the evaporation rate as it does not account for the limited capacity of the carrier gas to absorb

$$\Omega_D = \frac{A}{(T^*)^B} + \frac{C}{e^{DT^*}} + \frac{E}{e^{FT^*}} + \frac{G}{e^{HT^*}}$$
 (6)

Our second approach for estimating the theoretical acetone vapor mass at late times is to treat the system as a constant pressure closed system (no mixing) coming to phase equilibrium. A simple psychrometric calculation will show that the carrier gas cannot completely absorb the liquid acetone mass as vapor before becoming saturated. Based on the initial concentration of acetone vapor in the air, 30 % of the liquid acetone mass can evaporate before the air is saturated with vapor. This method underpredicts the evaporation of the acetone droplets but given that it does not consider the mixing of the interface gas and the surrounding dry gas, it provides a reasonable lower bound. If mixing is considered, the acetone evaporation rates observed in the experiments (59.48 %) may be reasonable.

6. Conclusions

New experimental equipment and image processing techniques to study acetone vapor concentration in SDMI experiments have been developed and presented in this paper. SDMI experiments

were run and acetone vapor measurements taken at two times after the shock acceleration. Analysis of these images was performed to find the amount of evaporation occurring for the bulk droplet field. Nonetheless, it is acknowledged that two data points in time are insufficient to fully understand and describe the physics behind the evaporation rate in the SDMI. However, these initial experiments provide the first measurement of evaporation rates in a shock-driven multiphase flow with hydrodynamic mixing and show the potential of our new experimental methods and equipment. It is noted that while this method is based on previous well-validated acetone vapor fluorescence measurements, further validation under dynamic conditions is desirable. Future work will seek to provide further validation and more extensive data on the temporal evolution of the SMDI interface.

The new multiphase interface, using acetone droplets, was shown to evolve similar to our previous work with water droplets Middlebrooks et al. (2018). PIV measurements produced an estimate for the strength of the primary vortices, where the strength and organization of the vortices were similar to those found in previous RMI work Orlicz et al. (2013) and our previous simulation work for smaller water particles Black et al. (2017); Paudel et al. (2018). While the interface morphology of the acetone droplet field is similar to our previous work with water droplets of the same size (10.7 µm), the breakup dynamics are different. The 10.7 μ m-diameter water droplets (We = 32) likely breakup by the bag-breakup mechanism, while the acetone droplets of 10.7 μ mdiameter (We = 130.5) break into smaller child droplets through the sheet-stripping mechanism. This leads to the acetone droplets evaporating faster (until the carrier gas saturates), and coming to velocity equilibrium faster.

Using two simple evaporation models, we have observed that evaporation occurs much faster than predicted by 1-D steady models like the D^2 model. Further, the mixing of the multiphase field with the surrounding dry gas increases evaporation beyond that predicted for a closed system in phase equilibrium. From the two evaporation estimates discussed, it can be concluded that some combination of both scenarios is occurring. In the core of the interface fluid, the multiphase mixture is shielded from the surrounding dry gas and evaporation ceases when the carrier gas becomes saturated with acetone vapor. At the outer edge, where the interface fluid mixes with the surrounding dry gas, the D^2 model is more applicable, and the droplets evaporate quickly as they are mixed into the dry gas. As a result, the bulk evaporation rate for the droplet cloud is limited by the mixing induced by the SDMI.

Declaration of competing interest

The authors declare that they have no known competing financial interests or personal relationships that could have appeared to influence the work reported in this paper.

CRediT authorship contribution statement

Vasco Duke-Walker: Methodology, Validation, Formal analysis, Investigation, Writing - original draft. **Roy Allen:** Formal analysis, Writing - review & editing. **W. Curtis Maxon:** Writing - review & editing. **Jacob A. McFarland:** Supervision, Project administration, Funding acquisition, Writing - review & editing.

Acknowledgment

The authors would like to thank the National Science Foundation (NFS) for their funding through grant number 1844603. The authors would also like to thank our laboratory coworkers Calvin Young, John Middlebrooks, Sahir Almuna, Nathan Crum, and Joshua Stiff for their support and guidance over the course of this work.

References

- Black, W.J., Denissen, N.A., McFarland, J.A., 2017. Evaporation effects in shock-driven multiphase instabilities. J Fluids Eng 139 (7).
- Christopher, R.W., 2012. Turbulent Mixing Measurements in the Richtmyer-Meshkov Instability. University of Wisconsin- Madison, Nuclear Engineering and Engineering Physics Ph.d. dissertation.
- Colarossi, M., Trask, N., Schmidt, D.P., Bergander, M.J., 2012. Multidimensional modeling of condensing two-phase ejector flow. Int. J. Refrig 35 (2), 290–299.
- Crowe, C.T., Schwarzkopf, J.D., Sommerfeld, M., Tsuji, Y., 2011. Multiphase flows with droplets and particles. CRC press.
- Dahal, J., McFarland, J.A., 2017. A numerical method for shock driven multiphase flow with evaporating particles. J Comput Phys 344, 210–233.
- Dai, Z., Faeth, G.M., 2001. Temporal properties of secondary drop breakup in the multimode breakup regime. Int. J. Multiphase Flow 27 (2), 217–236. doi:10.1016/ S0301-9322(00)00015-X.
- Duke-Walker, V., Maxon, W.C., Almuhna, S.R., McFarland, J.A., n.d. Evaporation and breakup effects in the shock-driven multiphase instability. J Fluid Mech. Submitted for publication.
- Goossens, H., Cleijne, J., Smolders, H., Van Dongen, M., 1988. Shock wave induced evaporation of water droplets in a gas-droplet mixture. Exp Fluids 6 (8), 561–568.
- Guildenbecher, D., López-Rivera, C., Sojka, P., 2009. Secondary atomization. Exp Fluids 46 (3), 371.
- Hanson, T.C., Davidson, D.F., Hanson, R.K., 2007. Shock-induced behavior in micronsized water aerosols. Physics of Fluids 19 (5), 056104.
- Hirschfelder, J.O., Curtiss, C.F., Bird, R.B., Mayer, M.G., 1964. Molecular theory of gases and liquids, 165. Wiley New York.
- Hsiang, L.-P., Faeth, G.M., 1992. Near-limit drop deformation and secondary breakup. Int. J. Multiphase Flow 18 (5), 635–652.
- Kothakapa, R.V.R., 2017. Design of experimental apparatus for generation and measurement of an aeroso. University of Missouri, Mechanical and Aerospace Engineering Master dissertation.
- Kozasa, T., Nozawa, T., Tominaga, N., Umeda, H., Maeda, K., Nomoto, K., 2009. Dust in supernovae; formation and evolution. arXiv preprint arXiv:0903.0217.
- Lu, F.K., Braun, E.M., 2014. Rotating detonation wave propulsion: experimental challenges, modeling, and engine concepts. J. Propul. Power 30 (5), 1125–1142.
- Marble, F.E., 1970. Dynamics of dusty gases. Annu Rev Fluid Mech 2 (1), 397-446.

- McFarland, J.A., Black, W.J., Dahal, J., Morgan, B.E., 2016. Computational study of the shock driven instability of a multiphase particle-gas system. Physics of Fluids 28 (2), 024105.
- McFarland, J.A., Hagenmaier, M., 2018. Computational study of shock-driven multiphase mixing in scramjet conditions. AIAA Journal 56 (10), 4004–4015.
- Meng, J.C., Colonius, T., 2018. Numerical simulation of the aerobreakup of a water droplet. J Fluid Mech 835, 1108.
- Middlebrooks, J.B., 2019. Shock Tube Experimentation Utilizing Advance Diagnostics for the Study of an Impulsively Accelerated Multiphase Cylinder. University of Missouri-Columbia, Mechanical and Aerospace Engineering Ms dissertation.
- Middlebrooks, J.B., Avgoustopoulos, C.G., Black, W.J., Allen, R.C., McFarland, J.A., 2018. Droplet and multiphase effects in a shock-driven hydrodynamic instability with reshock. Exp Fluids 59 (6). doi:10.1007/s00348-018-2547-7.
- Mohammad, M., 2019. Effects Of Initial Conditions And Mach Number On Turbulent Mixing Transition Of Shock-Driven Variable-Density Flow. Georgia Institute of Technology, Mechanical and Aerospace Engineering Phd dissertation.
- Neufeld, P.D., Janzen, A., Aziz, R., 1972. Empirical equations to calculate 16 of the transport collision integrals ω (l, s)* for the lennard-jones (12–6) potential. J Chem Phys 57 (3), 1100–1102.
- Nist, 2020. Chemistry webbook. In: Linstrom, P., Mallard, W. (Eds.), NIST standard reference database number 69. National Institute of Standards and Technology.
- Orlicz., G., 2012. Incident shock Mach number effects on Richtmyer-Meshkov mixing with simultaneous density and velocity measurements. University of New Mexico, Mechanical Engineering Ph.d. dissertation.
- Orlicz, G.C., Balasubramanian, S., Prestridge, K.P., 2013. Incident shock mach number effects on richtmyer-meshkov mixing in a heavy gas layer. Physics of Fluids 25, 1070–6631.
- Paudel, M., Dahal, J., McFarland, J., 2018. Particle evaporation and hydrodynamics in a shock driven multiphase instability. Int. J. Multiphase Flow 101, 137–151.
- Pilch, M., Erdman, C., 1987. Use of breakup time data and velocity history data to predict the maximum size of stable fragments for acceleration-induced breakup of a liquid drop. Int. J. Multiphase Flow 13 (6), 741–757.
- Poling, B.E., Prausnitz, J.M., O'connell, J.P., et al., 2001. The properties of gases and liquids, 5. Mcgraw-hill New York.
- Theofanous, T., Li, G., 2008. On the physics of aerobreakup. Physics of fluids 20 (5), 052103.
- Thielicke, W., Stamhuis, E., 2014. Pivlab-towards user-friendly, affordable and accurate digital particle image velocimetry in matlab. J Open Res Softw 2 (1).
- Thurber, Mark Clinton, 1999. Acetone Laser-Induced Fluorescence for Temperature and Multiparameter Imaging In Gaseous Flows. Stanford University, Mechanical Engineering Ph.d. dissertation.
- Vorobieff, P., Anderson, M., Conroy, J., White, R., Truman, C.R., Kumar, S., 2011. Vortex formation in a shock-accelerated gas induced by particle seeding. Phys. Rev. Lett. 106 (18), 184503.
- Wert, K., 1995. A rationally-based correlation of mean fragment size for drop secondary breakup. Int. J. Multiphase Flow 21 (6), 1063–1071.
- Wróblewski, W., Dykas, S., Gardzilewicz, A., Kolovratnik, M., 2009. Numerical and experimental investigations of steam condensation in lp part of a large power turbine. J Fluids Eng 131 (4).